


Morphological stripe-bubble transition in remanent magnetic domain patterns of Co/Pt multilayer films and its dependence on Co thickness

Karine Chesnel,^{1,*} Andrew S. Westover,^{1,†} Carson Richards,¹ Brittini Newbold,¹ Matthew Healey,¹ Lauren Hindman,¹ Berg Dodson,¹ Kelsey Cardon,¹ David Montealegre,¹ Jeremy Metzner,¹ Tobias Schneider,² Benny Böhm,³ Fabian Samad,³ Lorenzo Fallarino,² and Olav Hellwig^{2,3}

¹*Department of Physics and Astronomy, Brigham Young University, Provo, Utah 84602, USA*

²*Institute of Ion Beam Physics and Materials Research, Helmholtz-Zentrum Dresden-Rossendorf, Bautzner Landstrasse 400, 01328 Dresden, Germany*

³*Institute of Physics, Chemnitz University of Technology, D-09107 Chemnitz, Germany*

 (Received 25 August 2017; revised manuscript received 3 October 2018; published 4 December 2018)

We report a morphological transition in the magnetic domain pattern exhibited by perpendicular anisotropy ferromagnetic [Co/Pt]₅₀ multilayer films at room temperature and remanence. We found that the remanent magnetic domain morphology and the associated domain density, defined as the number of domains of a given magnetization direction per area, strongly depend on the magnetic history. When the magnitude of the previously applied external field approaches a specific value, typically 75–95% of the saturation field, the magnetic pattern, which generally forms a maze of interconnected stripe domains, decays into a shorter stripe pattern, and the domain density increases. We mapped out this morphological transition as a function of the previously applied field magnitude as well as the Co thickness. We found that a Co thickness close to 30 Å yields the highest domain density with the formation of a pure bubble domain state. Three-dimensional micromagnetic simulations confirm the formation of a pure bubble state in that parameter region and allow an estimation of the perpendicular anisotropy (here 2×10^5 J/m³ for an input magnetization of 1080 kA/m), as well as the interpretation of distinct features of the samples' hysteresis loop based on the corresponding domain pattern.

DOI: [10.1103/PhysRevB.98.224404](https://doi.org/10.1103/PhysRevB.98.224404)

I. INTRODUCTION

Ferromagnetic thin films with perpendicular magnetic anisotropy (PMA) are of interest for both fundamental and applied research. In PMA systems, magnetic anisotropy and magnetostatic self-interaction are opposing each other, causing nonuniform magnetization states at the microscale and nanoscale [1–12]. In the limit of ultrathin magnetic films, this competition sometimes leads to the formation of specific magnetic textures as a pathway to minimize the total energy, consisting of either vortices [13–15] or skyrmions [16–19]. While both were proposed to be employed in magnetic memory devices [20–21], the main types of magnetic structures for developing magnetic memory technologies have been bubble and stripe domain patterns occurring in thicker PMA films [22–29]. Indeed, compared to in-plane (IP) magnetic materials, PMA systems exhibit a far richer variety of magnetic structures, the different shape and geometry of which are strongly influenced by their delicate energy balance. While the magnetic domain patterns exhibited by PMA systems are interesting morphological systems, it is important to understand their underlying formation process. Indeed, understanding how the magnetic domain structures form at the microscopic scale will allow the identification and control of microscopic

magnetic transitions. Also, it may allow the stabilization of domain textures even in thick systems without the need of additional symmetry-breaking energy contributions such as, for example, the Dzyaloshinskii-Moriya interaction [30,31].

In the past decades, various observations of magnetic domain patterns in thin PMA ferromagnetic films have established some correlations between the domain shape or size and the film thickness [8,12,25]. If the film is smooth and thin enough, the magnetic domains often take the shape of stripes the characteristic width of which is typically about 50–200 nm. The corresponding length may reach up to many microns, depending on the thickness and microstructure of the film but also on the magnetic field history that the material was exposed to. When long enough, the stripe domains of opposite magnetization directions interlace and yield a maze pattern. When they are short, on the order of 100 nm, the domains take the shape of bubbles, thus forming a pattern of bubblelike domains of one magnetization direction embedded in a single background domain made of the opposite magnetization direction. Moreover, if the PMA films exhibit little or no remanence (i.e., no net magnetization in the absence of an external magnetic field), the total area covered by domains of the two opposite magnetization directions is approximatively equal. Such a balanced state may, however, be microscopically achieved by a rich variety of different domain pattern morphologies. In the case of out-of-plane (OOP) magnetic field application, the remanent pattern might consist in the extreme cases of either a completely interconnected maze domain pattern or a lattice of isolated bubbles [32].

*Corresponding author: kchesnel@byu.edu

†Present address: Oak Ridge National Laboratory, Oak Ridge, Tennessee 37830, USA.

The aim of this paper is to understand the morphological transition between the two above-mentioned maze and bubble magnetic domain patterns while varying certain system parameters. In particular, we study the dependence of the magnetic domain morphology at remanence and its associated domain density with respect to both the thickness of the magnetic film and the magnitude of a previously applied OOP magnetic field. For our investigation, we employ Co/Pt multilayer thin films with a specific set of structural parameters, for which the net magnetization at remanence is close to zero [12]. In our paper, we image the magnetic domain patterns at remanence after applying an OOP magnetic field of varying magnitude. We then map out a morphological transition between mazelike and bubblelike domain patterns as a function of previously applied field and Co thickness. By performing this detailed study, we are able to identify an optimal magnetic field and Co thickness, for which the density of reverse magnetic domains at remanence is extraordinarily enhanced.

The paper is organized as follows. In Sec. II we describe the fabrication as well as the room-temperature magnetic properties of our PMA Co/Pt multilayer thin films. In Sec. III, we explain the methodology used to study the remanent magnetic domain patterns. Section IV shows the results for various Co thicknesses, including a magnetic domain density study as a function of the previously applied magnetic field. In Sec. V, a map of the morphological magnetic transition is shown, discussed, and interpreted. Section VI shows results of three-dimensional micromagnetic simulations that allow to better understand the observed reversal behavior and to extract the approximate anisotropy value for the sample, which reveals the most extensive bubble array within our series. Finally, Sec. VII provides a summary of the accomplished results and a general conclusion drawn from our work.

II. MATERIAL

Our ferromagnetic PMA thin films consist of $[\text{Co}(t_{\text{Co}} \text{ \AA})/\text{Pt}(7 \text{ \AA})]_{50}$ multilayers, which were deposited on Si wafers with a native SiO_x layer, a 15 Å Ta seed layer, and a 200 Å Pt buffer layer and covered by a capping layer of 23 Å of Pt, as illustrated in Fig. 1(a). Each multilayer includes 50 repeats of a bilayer made of 7 Å of Pt and t_{Co} Å of Co, where $4 \leq t_{\text{Co}} \leq 60 \text{ \AA}$. The multilayers were fabricated by using an AJA ATC 2200 sputter system in a multisource confocal sputter-up geometry with a target-substrate distance of 4–6 in. and a base pressure lower than 3×10^{-8} Torr. During the deposition, a low Argon pressure of 3×10^{-3} Torr was used and the substrate was rotated at about 3 Hz in order to obtain high uniformity. Moreover, all the depositions were performed at elevated temperature, $T = 523 \text{ K}$, in order to enhance the fcc (111) texturing of the Pt underlayer, which consequently promotes a fcc (111) texture throughout the Co/Pt multilayer structures [33]. Co was sputtered at 250 W with a deposition rate of 1.8 Å/s, whereas Pt was sputtered at 100 W with a deposition rate of 2 Å/s. The structural characterization performed by x-ray diffraction confirms that both the 20-nm Pt seed layers and the Co/Pt multilayer films have a fcc (111) texture, with broad rocking peak widths of about 12° full width at half maximum (FWHM).

The PMA in our multilayers is achieved via the combination of texturing and layering. In fact, the preferential orienta-

tion of the magnetization in a single layer of Co sandwiched in between two Pt layers strongly depends on the Co thickness t_{Co} . In such Co/Pt multilayer systems, the magnetocrystalline anisotropy and the interface anisotropy are generally opposing the shape anisotropy caused by the magnetostatic self-interaction. This generates nonuniform microscopic magnetization states as a pathway to minimize the total magnetic energy. At some critical thicknesses t_{Co} , the magnetization changes its preferential orientation due to the predominance of shape anisotropy over the magnetocrystalline and interface anisotropies, and vice versa. If the thickness t_{Co} of a single Co layer is below $\sim 16 \text{ \AA}$,¹ the interface anisotropy overcomes the shape anisotropy, resulting in an OOP magnetization independent of the number of repeats N [4,7,33–40]. However, if the Co thickness is larger than $\sim 16 \text{ \AA}$, the shape anisotropy, which is constant and equal to $2\pi M_s^2$ in the low thickness regime (where M_s is the magnetization at saturation) [41], starts to dominate the interface anisotropy, which scales with the inverse thickness [7], and the magnetization turns IP. A convenient way to visualize this crossover is by plotting the product of the effective anisotropy K_{eff} (as defined in Ref. [7]) and t_{Co} as a function of t_{Co} itself, leading to a linearly decreasing behavior as shown in Fig. 1(b). Here, a positive K_{eff} leads to an OOP magnetization, and a negative K_{eff} corresponds to an IP magnetization.

On the other hand, when t_{Co} further increases to far larger values, the magnetization eventually switches again towards the OOP direction. This second reorientation transition is caused by a dominance of the perpendicular magnetocrystalline anisotropy over the shape anisotropy, since for an OOP domain state the demagnetization energy per volume is scaling inversely with the thickness in the high thickness regime [42], whereas the magnetocrystalline anisotropy is constant (and zero except for the domain walls). This second transition was predicted by Kittel [43] with subsequent extensions [41,42] of his theoretical considerations, and identified experimentally later on [44–50]. Figure 1(c) displays the free energies (per unit area) of an IP single domain configuration (dark yellow dotted line) and of an OOP multidomain configuration (blue dashed line) as a function of t_{Co} . A crossover from IP to OOP occurs at $t_{\text{Co}} \approx 500 \text{ \AA}$ (in a multilayer, this corresponds to the total integrated Co thickness $t_{\text{Co,total}} = N t_{\text{Co}}$). The lines in Fig. 1(c) are an adaptation from Ref. [42]. Since the magnetocrystalline anisotropy contribution is positive and constant for an IP domain, the associated energy per unit area varies linearly and quickly with t_{Co} , hence causing an intersection with the very slowly increasing OOP line. There is a fundamental difference with respect to the low thickness transition displayed in Fig. 1(b): the crossover in the high thickness regime can only occur in the presence of OOP magnetocrystalline anisotropy, which in cobalt can be

¹The transition $K_{\text{eff}}(t_{\text{Co}}) = 0$ strongly depends on the effectiveness of the magnetic/nonmagnetic interface area, which can be affected by roughness, formation of interface alloys, or discontinuities of the thin layers. The quantity $K_{\text{eff}} t_{\text{Co}}$ actually becomes nonlinear at small Co thicknesses, but with our chosen range for t_{Co} this effect is not visible in the figure and is not further explored in this paper.

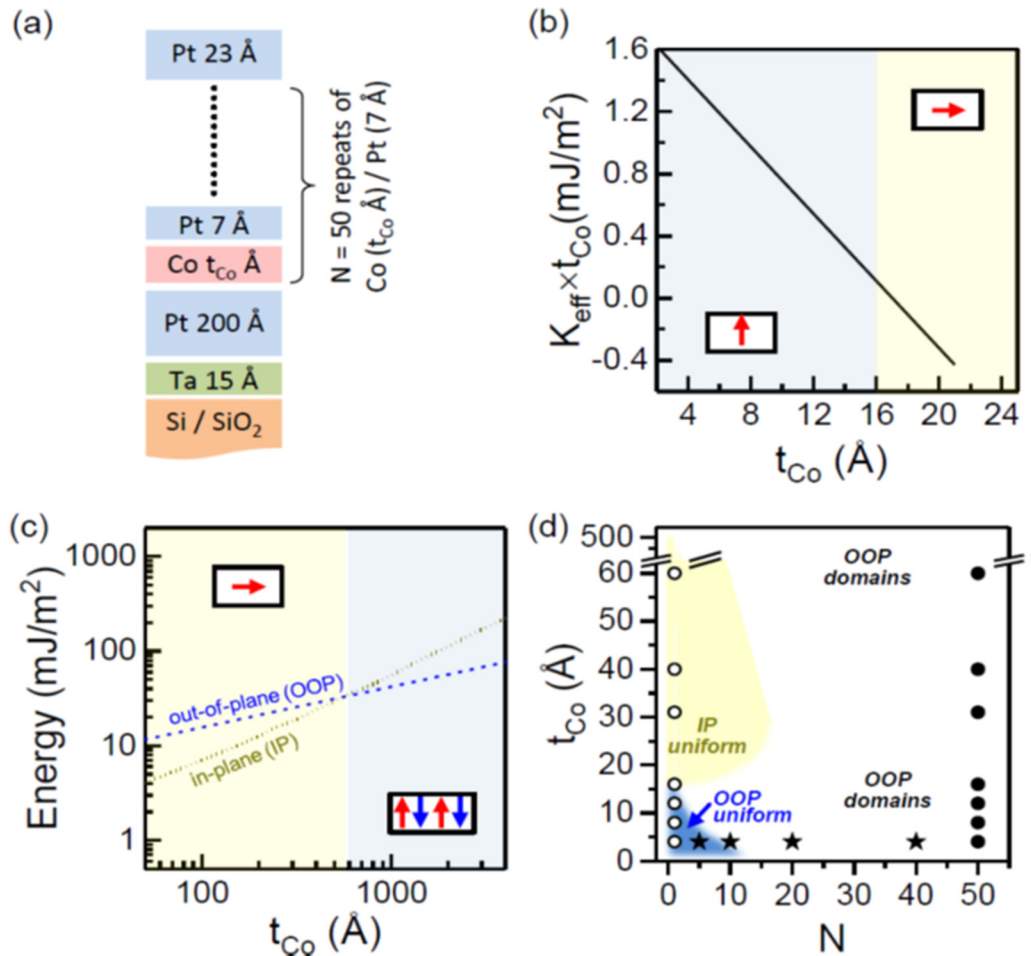


FIG. 1. (a) Sketch of the multilayer structure: Ta(15 Å)/Pt(200 Å)/[Co(t_{Co})/Pt(7 Å)]₅₀/Pt(23 Å) where $t_{\text{Co}} = 4, 8, 12, 16, 25, 31, 40,$ and 60 Å. (b) Effective anisotropy energy density multiplied by the individual Co layer thickness vs the individual Co layer thickness itself of Co/Pt multilayers plotted as a straight (black) line. Data are adapted from Ref. [7]. (c) Free-energy density vs Co thickness for single-domain IP (short-dotted dark yellow line) and multidomain OOP (blue dashed line) configurations, adapted from Ref. [42]. The insets in (b), (c) illustrate the overall preferential orientation of the magnetization of the Pt/Co/Pt systems for the different Co thicknesses. (d) Schematic illustration of the remanent magnetic ground-state configuration in [Co(t_{Co})/Pt(7 Å)]_N multilayers depending on N and t_{Co} , based on experimental observations [12,23–28,39,40,42,44–49]. The open dots correspond to Pt/Co(t_{Co})/Pt trilayer structures ($N = 1$), whereas the filled dots refer to [Co(t_{Co})/Pt(7 Å)]₅₀ multilayers ($N = 50$). The stars correspond to samples from Ref. [12] with [Co(4 Å)/Pt(7 Å)]_N structure. While for low N we observe a transition from uniform OOP to OOP domains via uniform IP when the individual Co layer thickness increases, this transition is suppressed at higher N , such that for $N = 50$ only OOP domain states are observed for all Co thicknesses.

achieved by adopting either the fcc (111) or the hcp (0001) crystallographic orientation.²

According to the above discussion, the thickness range explored in our paper apparently suggests that our samples should experience the OOP to IP reorientation transition displayed in Fig. 1(b). However, because of their multilay-

ered structure, the magnetization in our films remains OOP throughout the entire range of Co thicknesses. An illustration of this effect is depicted in Fig. 1(d), which shows a schematic illustration of the room-temperature magnetic ground state of the [Co(t_{Co})/Pt(7 Å)]_N system, combining various studies as a function of the thickness of the individual cobalt layer t_{Co} and the number of Co/Pt bilayer repetitions N .³

²Even though the degree of texturing in our films is somewhat lower (FWHM = 12° angular spread in the crystallographic plane alignment) than what was observed [11] in previously studied materials (FWHM = 5°–10°), the magnetocrystalline energy term is still present. Decreasing the degree of texturing induces a slight lowering of the crystalline perpendicular anisotropy. Consequently the window for the IP phase gets slightly larger, i.e., the crossover which normally occurs at $t_{\text{Co}} = 16$ Å shifts towards slightly lower thicknesses, whereas the second reorientation transition (at $t_{\text{Co, total}} \approx 500$ Å) moves toward slightly higher thicknesses due to a higher M_S/K ratio.

³Although the schematic illustration of the magnetic ground-state configuration is based on many experimental observations [12,23–28,39,40,42,44–49], it is far from the present paper's intention to provide an exact determination of phase lines and boundaries. We are conscious about the strong dependence on the material parameters as well as the microstructural quality of the samples. The schematic illustration is only intended to provide a qualitative overview of the various phases present and their approximate extent depending on t_{Co} and N .

The open dots correspond to the Pt/Co(t_{Co})/Pt ($N = 1$) structure, which implies a thickness driven reorientation transition from uniform OOP towards uniform IP for $t_{\text{Co}} \gtrsim 16 \text{ \AA}$. Interestingly, this transition occurs via a canted phase [51–53].

In our case, however, because of the $N = 50$ repeats of the Co/Pt bilayers, such an OOP/IP/OOP reorientation as for $N = 1$ does not occur. The IP phase window, which opens for $16 \lesssim t_{\text{Co}} \lesssim 500 \text{ \AA}$ with $N = 1$, is completely suppressed for $N = 50$ and the magnetization stays perpendicular for all Co thicknesses. Indeed, the total Co thickness now corresponds to 50 times the thickness of a single Co layer. When multiple Co layers of individual thickness $t_{\text{Co}} > 16 \text{ \AA}$ are stacked together and if the total thickness $t_{\text{Co, total}}$ exceeds $\sim 500 \text{ \AA}$ (which is the case when $N = 50$), the crystalline fcc (111) texture dominates and creates a net overall OOP anisotropy, as confirmed by Fig. 1(c). On the other hand, for individual Co thicknesses $t_{\text{Co}} < 16 \text{ \AA}$, the strong interface anisotropy, yielding the OOP magnetization for $N = 1$, is also preserved for all higher N . Then, since the magnetostatic energy per volume is constant for small N and decreasing for high N due to domain formation, the shape anisotropy never dominates in such multilayers for any N . Consequently, an OOP preferential orientation of the magnetization is obtained for the entire Co thickness range explored in this paper.

In order to predict the rough shape of the uniform IP phase area in the t_{Co} versus N schematic illustration [Fig. 1(d)] beyond the well-known case of $N = 1$, we took into consideration that the transitional Co thickness at the bottom phase boundary between IP state and OOP state (starting for $N = 1$ at $t_{\text{Co}} \sim 16 \text{ \AA}$) should steadily (but slowly) increase with the number of repeats N as the magnetocrystalline anisotropy energy increases with the total Co thickness, which itself increases with N . However, in this region the interface anisotropy energy still dominates but remains constant for a fixed t_{Co} and the total Co thickness is still far away from the critical value of 500 \AA , so the increase in the transitional Co thickness with N is slow for this regime. On the other hand, the transitional Co thickness at the top phase boundary between IP state and OOP state (starting for $N = 1$ at $t_{\text{Co}} \sim 500 \text{ \AA}$) should decrease quite rapidly with the number of repeats N . In this regime the total magnetic thickness and its magnetocrystalline anisotropy energy dominate, while the interface anisotropy energy plays only a minor role. In fact one can simply calculate through which points (N , t_{Co}) the phase boundary should go, given that the critical thickness of 500 \AA does not depend on N and the interface anisotropy energy increases only very slowly as we lower t_{Co} (which are both good assumptions). Hence the top phase boundary should penetrate through the points ($N = 1$, $t_{\text{Co}} \sim 500 \text{ \AA}$), ($N = 2$, $t_{\text{Co}} \sim 250 \text{ \AA}$), ($N = 3$, $t_{\text{Co}} \sim 165 \text{ \AA}$), \dots ($N = 17$, $t_{\text{Co}} \sim 30 \text{ \AA}$) \dots which all yield a total critical Co thickness of about 500 \AA . As a result we obtain the IP phase region in the schematic illustration of Fig. 1(d), which reaches out to its highest N values for an individual Co layer thickness of about 30 \AA .

Furthermore, a systematic study conducted by Hellwig *et al.* [12] on [Co(4 \AA)/Pt(7 \AA)] $_N$ multilayers for varying N is also shown in Fig. 1(d) (star symbols). For relatively thin films ($N = 5$) a uniform OOP magnetic state was found, producing a square shaped magnetization reversal curve with a well-defined switching field. When increasing the number of

repeats N , the reversal is characterized by domain nucleation, propagation, and annihilation. The high magnetostatic energy cost causes the uniform OOP state to be replaced by up and down stripe or mazelike domains at remanence, the characteristic width of which varies with total film thickness [12]. In this context we want to point out that the phase referred to as “uniform OOP” in Fig. 1(d) is theoretically still associated with a finite domain size. However, domains in this regime increase exponentially (very rapidly) in size as the magnetic thickness goes towards zero and therefore are usually much larger than the field of view (about 5–10 μm) in our microscopy analysis and thus can be considered practically as magnetically uniform (thin-film regime). Similarly the “OOP domain” state in Fig. 1(d) indicates the region where small sized stripe domains are present and where the domain width increases slowly with increasing total magnetic film thickness (square root increase in the thick-film regime) [12].

In order to confirm the exclusive OOP nature of our samples, we have investigated their magnetization behavior, i.e., measured their isothermal hysteresis loops. They were obtained via vibrating sample magnetometry (VSM) using an EZ7 Microsense and a Quantum Design physical properties measurement system. Figures 2(a)–2(h) show room-temperature normalized magnetization curves $M(H)$ measured for an OOP (red, thick curve) and IP (blue, thin curve) external magnetic field for different Co thicknesses. The OOP and IP curves, well documented in the literature [44–49], both show saturation plateaus at high-field values. In the OOP configuration, when the field magnitude is lowered back from positive saturation, the uniformly saturated state transforms into a mazelike stripe domain state via the formation of bubblelike domains of opposite magnetization orientation. This magnetization reversal process occurs rather abruptly at the nucleation field H_n , leading to a steep decline in the total magnetization M near $H = H_n$. As the field magnitude H is further reduced toward zero (remanence), the domain density as well as the average domain length increase initially. At remanence a tiny remaining hysteresis effect may exist as the result of sample imperfections. In the IP configuration, when the field strength is reduced back from positive saturation, lateral magnetization rotations occur driven by the demagnetization field in conjunction with the perpendicular magnetic anisotropy. This process yields the formation of stripe domain patterns at remanence. However, due to the direction of the previously applied field, a measurable IP magnetization component persists due to IP aligned domain walls, causing some hysteresis at low-field values. We, however, highlight that all the multilayers have in common that their OOP magnetization at remanence is close to zero ($M \approx 0$). All the different Co thickness films are therefore good candidates for exhibiting either mazelike or bubblelike domain patterns at remanence when performing OOP magnetic field sequences.

Intriguingly, when increasing the Co thickness t_{Co} , the OOP saturation field H_s^{OOP} and its IP counterpart H_s^{IP} evolve in a completely opposite fashion: H_s^{OOP} gradually increases with t_{Co} , whereas H_s^{IP} gradually decreases with t_{Co} . In contrast to the OOP case, when the magnetization reversal is driven by an IP magnetic field, there is no shape anisotropy to overcome in order to saturate the sample. Moreover, when increasing t_{Co} , the interface anisotropy energy term becomes less and less effective, weakening the total perpendicular anisotropy.

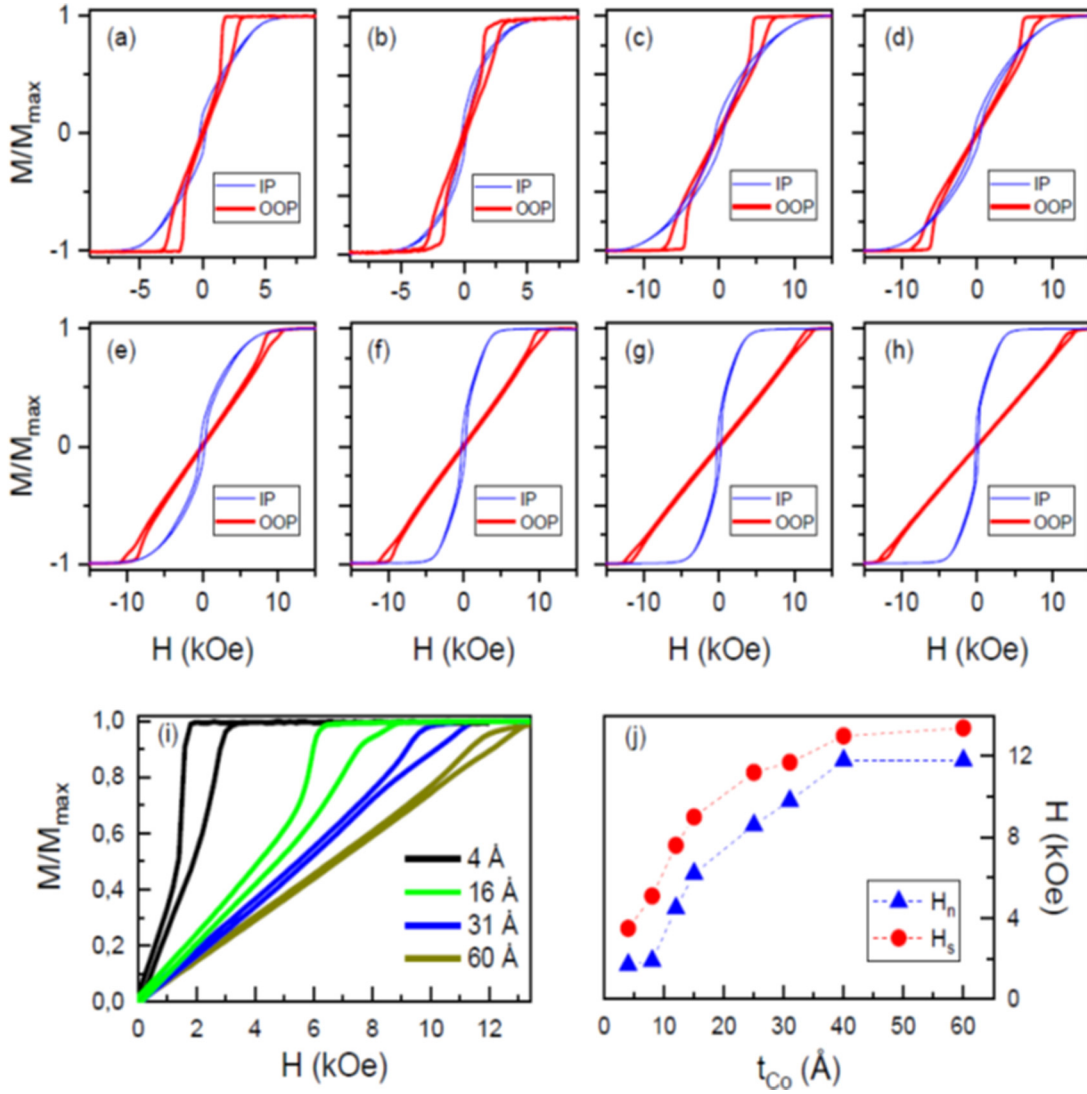


FIG. 2. VSM room-temperature hysteresis loops with the external magnetic field applied OOP (thick red line) or IP (thin blue line) for the eight different cobalt thicknesses $t_{\text{Co}} = 4$ Å (a), 8 Å (b), 12 Å (c), 16 Å (d), 25 Å (e), 31 Å (f), 40 Å (g), and 60 Å (h). Hereby, the VSM data are normalized to the magnetization at saturation M_s . (i) Zoomed-in view of the OOP normalized magnetization loops for the four selected Co thicknesses: 4, 16, 31, and 60 Å. (j) Plot of the OOP saturation field H_s (measured at the start of the plateau on the ascending branch) and nucleation field H_n (measured at the end of the plateau on the descending branch) as a function of t_{Co} .

Therefore, H_s^{IP} simply follows the reduction of the total perpendicular anisotropy, whereas H_s^{OOP} increases towards the $4\pi M_s$ value for cobalt, due to the increasing effectiveness of the domain driven reduction of the magnetostatic energy per volume in the remanent state [41], thus requiring a higher OOP field to saturate the material. This increase in H_s^{OOP} , as well as the accompanied increase in the nucleation field H_n with the Co thickness, can be seen in more detail in Fig. 2(i), where zoomed views of the OOP magnetization loops for various Co thicknesses are compared. Figure 2(j) displays H_s^{OOP} and H_n versus Co thickness, showing the discussed trend.

In summary of this material characterization section, we conclude that the entire set of the eight Co thicknesses shows an OOP easy magnetic axis and exhibits an OOP domain state at remanence, as highlighted in Fig. 1(d).

III. METHODS

In order to study the morphological magnetic transition from interconnected stripe to isolated bubble domains in our Co/Pt films, we mapped out the remanent magnetic domain pattern as a function of Co thickness and of magnetic field history. More specifically, we measured for each given Co thickness the density of isolated domains at remanence after OOP magnetization in $20 \times 20 \mu\text{m}^2$ fields of view. We then followed the evolution of this density (normalized to $100 \mu\text{m}^2$) while varying the magnitude of the previously applied OOP magnetic field.

For each Co thickness, we applied a series of OOP magnetization loops in a descending sequence of magnetic field strengths. The amplitude H_m of each loop was gradually decreased, starting at 90 kOe down to zero. After performing a magnetization loop of a specific amplitude $H_m (0 \rightarrow -H_m \rightarrow$

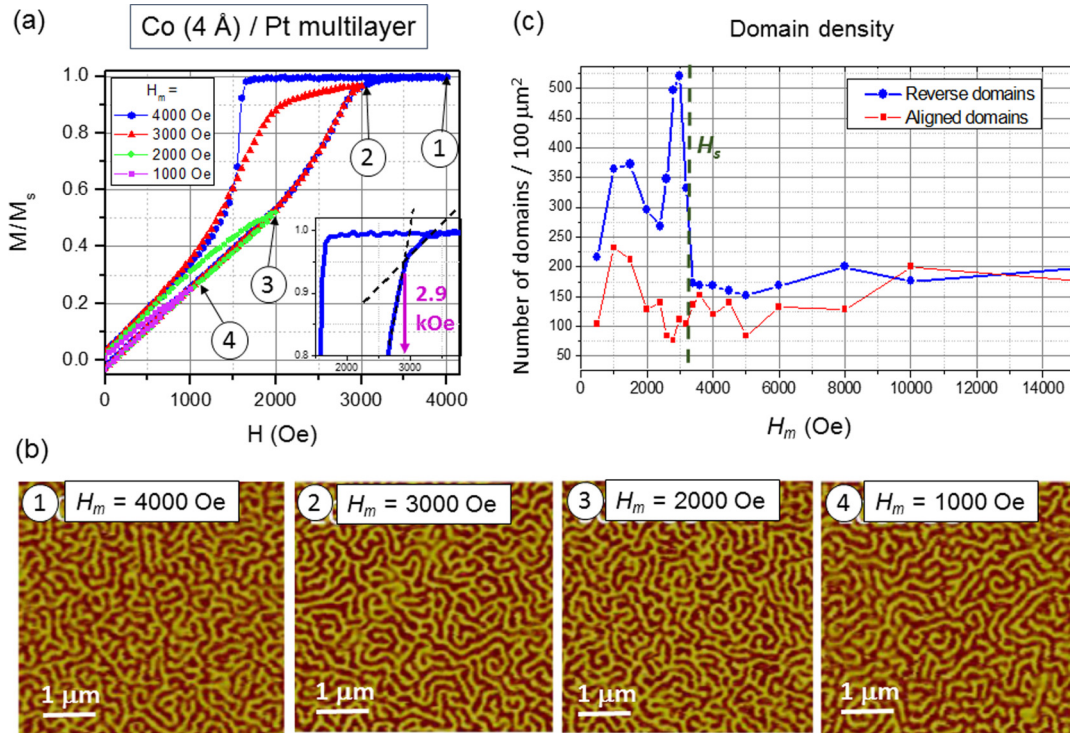


FIG. 3. Magnetization and imaging of the Co(4 Å)/Pt(7 Å) multilayer. (a) Set of magnetization curves selected from the descending external field series, measured via VSM, where $H_m = 4, 3, 2,$ and 1 kOe, respectively. Inset: Zoomed-in view of the 4-kOe loop highlighting the change of slope at 2.9 kOe. (b) Magnetic domain patterns measured at remanence corresponding to the four points indicated in (a). These images were collected via MFM and are $5 \times 5 \mu\text{m}^2$ in size. (c) Density of magnetic domains in the aligned and reverse directions as a function of H_m .

$+H_m \rightarrow 0$), the remanent magnetic domain pattern was imaged via magnetic force microscopy (MFM) using a Dimension 3100 Veeco Digital Instruments by Bruker and magnetic-coated etched silicon probe (MESP) type tips. Subsequently, domain densities were extracted computationally using a flood fill algorithm. The extracted densities for both the domains with their magnetization aligned with (“aligned domains”) as well as opposite to (“reverse domains”) the direction of the applied field were then plotted as a function of H_m .

This experimental procedure was applied to eight different Co thicknesses: $4, 8, 12, 16, 25, 31, 40,$ and 60 Å. Ultimately, the density of reverse domains is mapped out as a function of H_m and Co thickness. The resulting map reveals localized regions, where the density of the reverse domains is significantly enhanced, indicating a morphological magnetic transition. A specific field value H^* for which H_m yields a maximum reverse domain density n^* is extracted for each thickness. This maximum domain density n^* is then plotted as a function of Co thickness in order to determine the optimal Co thickness value yielding the overall highest domain density. In order to keep the paper compact, we will only show detailed results from the $4-, 16-, 31-,$ and 60-Å Co thicknesses.

IV. RESULTS

Magnetometry and MFM results for the 4-Å Co sample are shown in Fig. 3. A series of OOP magnetization loops selected from the descending field series where the magnitude H_m of the maximum applied field was decreased from 90 kOe down

to zero is displayed in Fig. 3(a). The shown loops correspond to $H_m = 4, 3, 2,$ and 1 kOe. At $H_m = 4$ kOe, the film is fully saturated (major loop) and at $H_m = 3$ kOe the film is just below saturation. In these two loops, the hysteretic region, i.e., the area between the ascending and the descending loop branches, is quite large with the 3-kOe minor loop already revealing a significantly altered nucleation due to previously incomplete saturation with remaining bubble domains still left in the system at H_m [54]. At lower H_m values (2 and 1 kOe), the film is significantly below saturation (minor loops) and the hysteretic region is smaller than for the major loop. Another interesting feature is a change of slope, which occurs just before saturation on the ascending branch of the major loop at about 2.9 kOe [Fig. 3(a) inset]. Interestingly, this point also marks a transition in domain morphology, as discussed in the next paragraph.

MFM images of the magnetic domain patterns were taken at remanence after each individual field reversal was applied. Figure 3(b) shows a selection of MFM images corresponding to $H_m = 4, 3, 2,$ and 1 kOe, respectively. For all the different H_m values, the film exhibits interlaced serpentine stripe domains of opposite magnetization direction. A careful statistical analysis of the domain pattern shows, however, that the density of the reverse domains actually changes significantly with H_m . The plot of the domain density versus H_m in Fig. 3(c) reveals a peak for the reverse domain density at a H_m value $H^* \sim 2.9$ kOe, where the density is increased from a 180 domains/ $100 \mu\text{m}^2$ baseline to about 520 domains/ $100 \mu\text{m}^2$. The value H^* turns out to be slightly

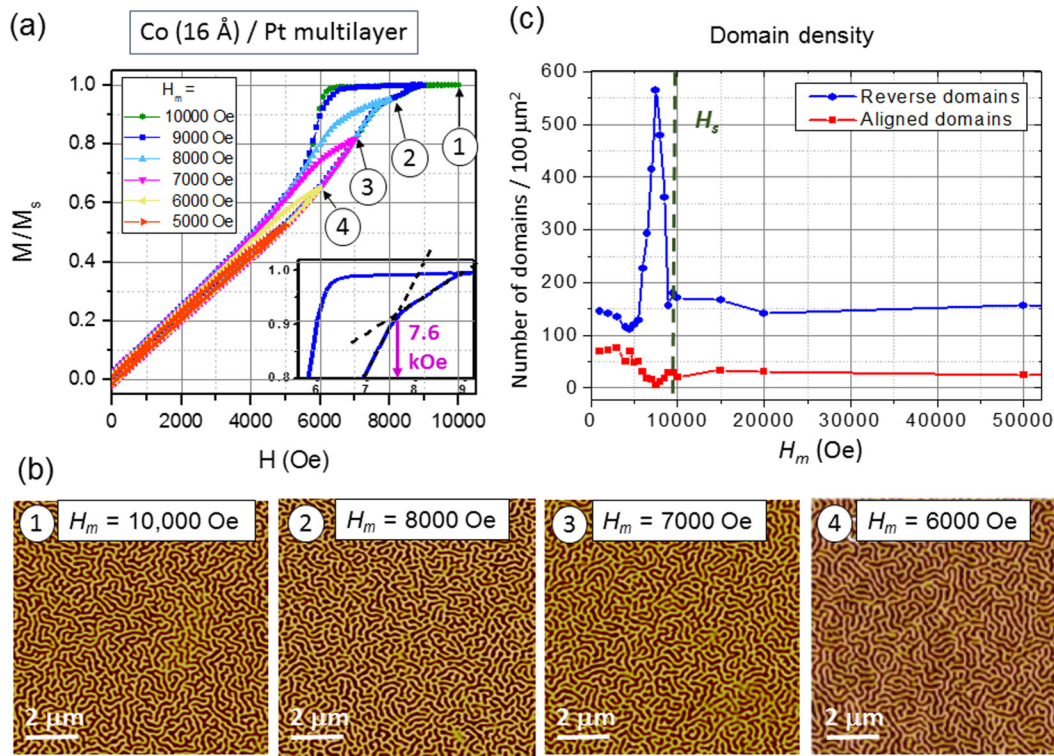


FIG. 4. Magnetization and imaging of the Co (16 Å)/Pt(7 Å) multilayer. (a) Set of magnetization loops selected from the descending external field series, measured via VSM. Inset: Zoomed-in view of the 9-kOe loop highlighting the change of slope at 7.6 kOe (b) Magnetic domain patterns measured at remanence corresponding to the four points indicated in (a) where $H_m = 10, 8, 7,$ and 6 kOe, respectively. These images were collected via MFM and are $10 \times 10 \mu\text{m}^2$ in size. (c) Density of magnetic domains in the aligned and reverse directions as a function of H_m .

below saturation $H_s = 3.07$ kOe [indicated by a dashed line on the graph of Fig. 3(c)], exactly where the slope change in the major loop occurs [inset of Fig. 3(a)]. It was shown in earlier studies [54,55] that this slope change just before saturation corresponds to a transition from contraction of stripe domains to annihilation of bubble domains.

When $H_m > H_s$, saturation has been reached prior to returning back to remanence. At saturation, all the magnetic domains have disappeared and the film is uniformly magnetized in one direction. It is expected that the subsequent domain pattern morphology at remanence and its associated domain density should not depend on the value of H_m anymore once $H_m > H_s$. The measured density value in that region is indeed nearly constant, at about $\sim 180 \pm 20$ domains/ $100 \mu\text{m}^2$. The observed domain density variation in the range of $\pm 20\%$ is attributed to experimental noise and due to the relatively limited field of view in this paper. A similar plateau in domain density for $H_m > H_s$ occurs for all the different Co thicknesses. This indicates that both macroscopic and microscopic saturations have been reached in the film when $H_m > H_s$. We conclude that at that stage no residual magnetic defects from the field reversal are left in the sample [54].

The behavior for the reverse domain density observed in the Co(4 Å)/Pt(7 Å) multilayer concurs with results obtained on the Co(8 Å)/Pt(7 Å) multilayer as described in detail in Ref. [56], for which the density of the reverse domains exhibits a peak located at $H_m = H^* = 4.5$ kOe and the maximum density was $n^* \sim 600$ domains/ $100 \mu\text{m}^2$. The similarity in

the behavior of the Co(4 Å)/Pt(7 Å) and the Co(8 Å)/Pt(7 Å) multilayers suggests that an enhancement in reverse domain density may also occur at higher Co thicknesses.

Figure 4 summarizes magnetization and imaging results for the 16-Å Co thickness. Figure 4(a) shows a set of minor OOP magnetization loops selected from the descending field series that was applied to the film. When $H_m < 5$ kOe, the minor loop shows very little hysteresis, indicating reversible magnetization processes. When $H_m > 5$ kOe, the loop opens and hysteresis starts to occur, indicating the onset of irreversible magnetization processes. The estimated saturation field is about $H_s = 8.9$ kOe. Figure 4(b) shows magnetic domain patterns collected at remanence after the application of a major loop ($H_m = 10$ kOe) and minor loops ($H_m = 8, 7,$ and 6 kOe, respectively). Here again, while the film exhibits at remanence interlaced domain patterns, we observe a peak in the reverse domain density for a particular H_m , as displayed in Fig. 4(c). The effect is even more pronounced than for the Co(4 Å)/Pt(7 Å) and the Co(8 Å)/Pt(7 Å) films. The density is here increased from a 150 ± 15 domains/ $100 \mu\text{m}^2$ baseline to a maximum value of 565 domains/ $100 \mu\text{m}^2$ occurring for $H_m = H^* \approx 7.5$ kOe. There, the average length of the stripe domains is significantly reduced. We note that, here again, H^* is slightly lower than the saturation field $H_s = 8.9$ kOe [marked by a dashed line in Fig. 4(c)]. Also, at H^* a slope change occurs on the ascending branch of the major hysteresis loop [Fig. 4(a) inset]. As for smaller Co thicknesses, this slope change corresponds to the aforementioned transition

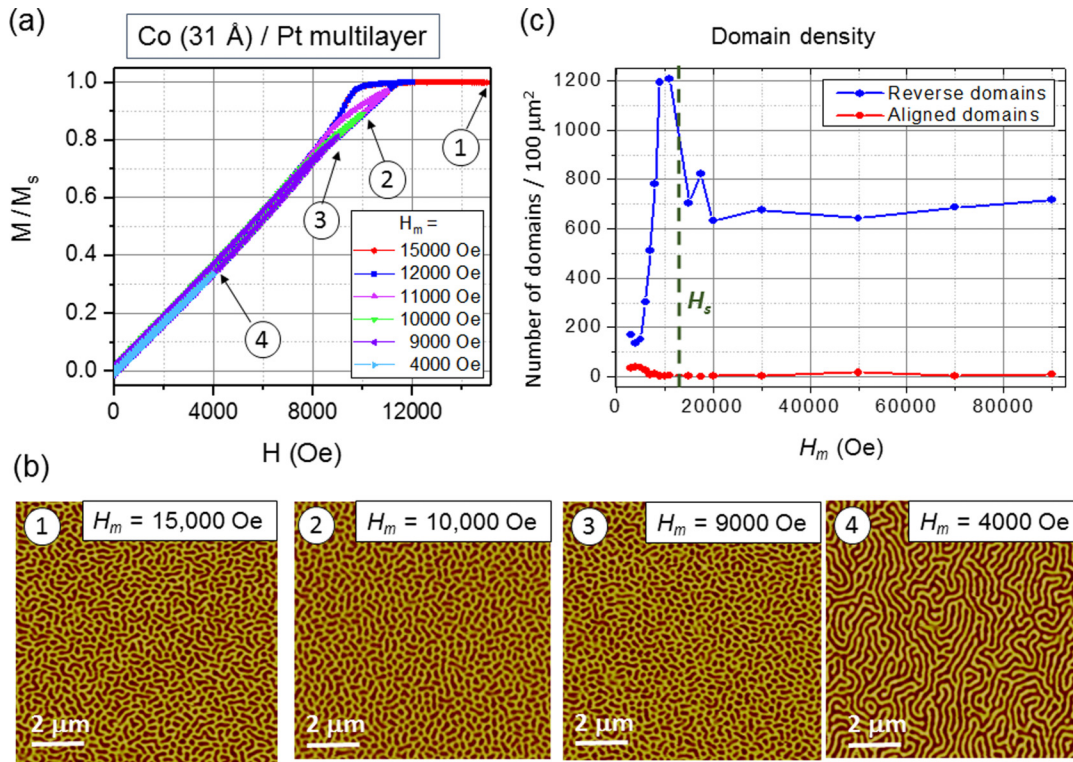


FIG. 5. Magnetization and imaging of the Co(31 Å)/Pt(7 Å) multilayer. (a) Set of magnetization loops selected from the descending external field series, measured via VSM. (b) Magnetic domain patterns measured at remanence corresponding to the four points indicated in (a) where $H_m = 15, 10, 9,$ and 4 kOe, respectively. These images were collected via MFM and are $10 \times 10 \mu\text{m}^2$ in size. (c) Density of magnetic domains in the aligned and reverse directions as a function of H_m .

from contraction of stripe domains to annihilation of bubble domains [54,55].

The measurements for the 31-Å Co thickness, in Fig. 5, show the most significant morphological changes. Figure 5(a) displays a set of minor magnetization loops selected from a descending OOP field series. The minor loops remain closed for an extended range of H_m values, all the way up to about 10 kOe. When $H_m > 10$ kOe, the loop opens slightly and a small hysteretic effect occurs towards the extremity, just below saturation. The saturation field is about $H_s = 11.4$ kOe. Figure 5(b) shows magnetic domain patterns collected at remanence after the application of a major loop ($H_m = 15$ kOe) and minor loops ($H_m = 10, 9,$ and 4 kOe, respectively). The pattern at $H_m = 15$ kOe shows a large number of reverse domains, that are significantly shorter in length than for other Co thicknesses when $H_m > H_s$. The associated density baseline at large H_m in the density plot in Fig. 5(c) is consequently much higher, about 680 ± 25 domains/ $100 \mu\text{m}^2$, than for thinner Co films, where the baseline was at about 150 domains/ $100 \mu\text{m}^2$. When H_m is decreased down to $H_m = 10$ kOe, which is slightly below saturation H_s , the reverse domains become even shorter in length to the point of taking the shape of round bubbles, thus forming a bubble pattern. The associated domain density significantly increases to nearly 1200 domains/ $100 \mu\text{m}^2$ at a peak H_m value of $H^* = 9.5$ kOe. As H_m is decreased to lower values, the shapes of the reverse domains transform from pure bubbles back to long stripes, and eventually form a pure maze pattern of interlaced stripe domains when $H_m < 4$ kOe. The associated reverse domain den-

sity at that stage is back down to about 170 domains/ $100 \mu\text{m}^2$. This significant decrease in density, from 1200 down to about 170 domains/ $100 \mu\text{m}^2$, a factor 7 lower, is remarkable.

For smaller Co thicknesses, a decrease in density also occurs when H_m is decreased from H^* to lower values, but the drop is not as strong (it typically drops by a factor 2–4). Also, for smaller Co thicknesses, the densities at low $H_m \ll H^*$ and at high $H_m \gg H^*$ somewhat match, converging at a value around 150–200 domains/ $100 \mu\text{m}^2$, which corresponds to an interlaced stripe maze state. Here, for the 31-Å Co thickness, the density at large $H_m \gg H^*$ is much higher (around 700 domains/ $100 \mu\text{m}^2$) than at low $H_m \ll H^*$ (around 150 domains/ $100 \mu\text{m}^2$). Interestingly, we also observe that the slope change just before saturation, which was previously pointed out for the 4 and 16 Å Co thicknesses, has nearly vanished. Instead the loop reveals an almost linear slope regime all the way from remanence to saturation. As we will later see from micromagnetic modeling, the steeper slope region that corresponds to an irreversible stripe contraction is replaced by a decay of stripes into (lines of) bubbles for thicker Co samples. This yields a less steep slope in the magnetization versus field curve. Therefore, the characteristic slope change typical for thinner Co samples (from contraction of stripes to contraction and annihilation of bubbles) is not observed for larger Co thicknesses.

Results for the 60-Å Co thickness are presented in Fig. 6. Compared to the 31-Å Co sample, the hysteretic area in Fig. 6(a) shrinks even further. The estimated saturation field is now $H_s \approx 13$ kOe. Figure 6(b) shows magnetic domain

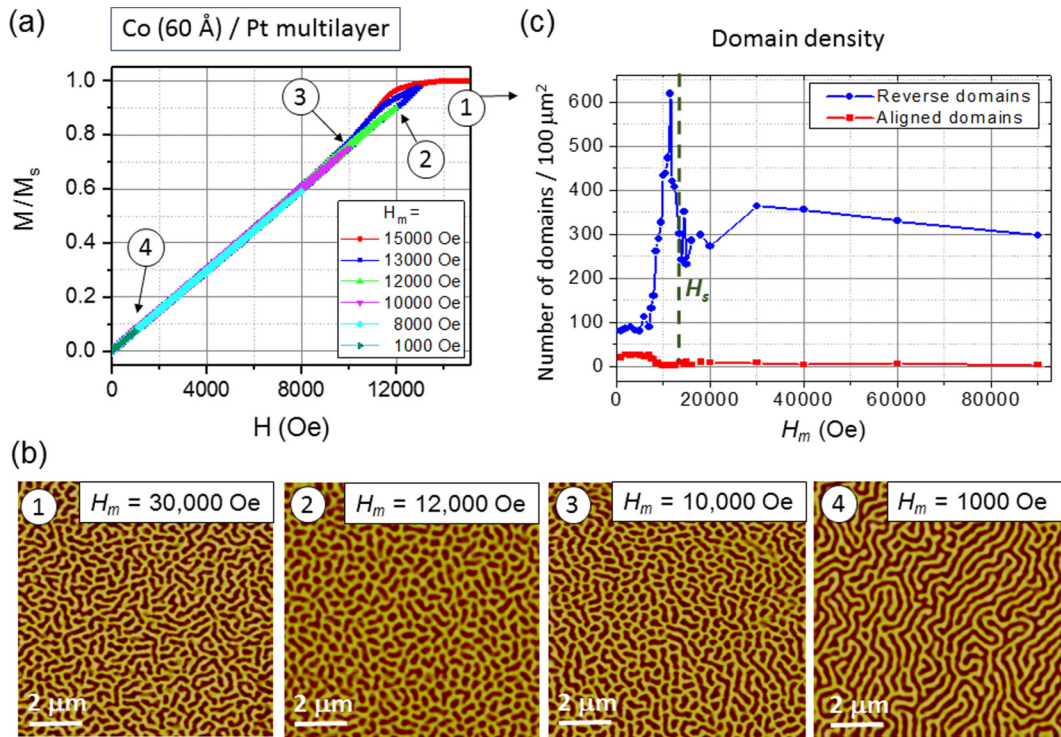


FIG. 6. Magnetization and imaging of the Co(60 Å)/Pt(7 Å) multilayer. (a) Set of magnetization loops selected from the descending external field series, measured via VSM. (b) Magnetic domain patterns measured at remanence corresponding to the four points indicated in (a) where $H_m = 30$, 12, 10, and 1 kOe, respectively. These images were collected via MFM and are $10 \times 10 \mu\text{m}^2$ in size. (c) Density of magnetic domains in the aligned and reverse directions as a function of H_m .

patterns collected at remanence after the application of a major loop ($H_m = 30$ kOe) and three minor loops ($H_m = 12$, 10, and 1 kOe, respectively). The pattern at $H_m = 30$ kOe shows a large number of reverse domains, that are significantly shorter in length than for Co thicknesses of 16 Å and less. The associated density of the reverse domains in Fig. 6(c) shows a baseline at high $H_m > H_s$ of about 335 ± 25 domains/ $100 \mu\text{m}^2$, which is twice as much as the 150 domains/ $100 \mu\text{m}^2$ baseline for the low Co thicknesses, but only about half of the observed density for the Co 31-Å thickness. When H_m is decreased down to below saturation ($H_m = 12$ kOe) the reverse domains become even shorter in length and form elongated bubbles. Here again, a peak domain density is observed. The peak occurs here at $H^* \approx 11.5$ kOe where the reverse domain density is increased to nearly 650 domains/ $100 \mu\text{m}^2$. For lower reverse field values H_m , the reverse domains elongate from the bubble shape back to long stripe shapes and form a maze pattern again, as illustrated for $H_m = 1$ kOe, and the density drops back down to about 85 ± 5 domains/ $100 \mu\text{m}^2$.

At a Co thickness of 60 Å the ascending hysteresis loop branch is in a completely linear slope regime all the way from remanence to saturation. Characteristic slope changes, such as those observed for the 4- and 16-Å Co thicknesses, are no longer visible for larger Co thicknesses. This evolution towards a more linear slope on the ascending hysteresis loop branch together with a reduced hysteretic area is discussed and interpreted in more detail in the micromagnetic simulation section below.

V. DISCUSSION

The variety of remanent domain patterns observed in the [Co/Pt]₅₀ multilayers confirms a morphological magnetic phase transition. For large Co thicknesses, the magnetic domain pattern at remanence gradually evolves from a short stripe pattern to a bubble-type pattern and finally to an interconnected mazelike pattern as the magnitude H_m of the previously applied OOP magnetic field is gradually reduced from beyond saturation down to remanence. In order to visualize this stripe-bubble transition, we map, in Fig. 7(a), the density of the reverse domains as a function of H_m and of Co thickness. To highlight important features, the density map is split into two parts: on the left side, a low-field map (covering the range $0 < H_m < 10.5$ kOe) with fine interpolating step size ($\Delta H_m = 1.5$ kOe); on the right side, a high-field map (covering the range $10 < H_m < 90$ kOe) with wider interpolating step size ($\Delta H_m = 20$ kOe). Both maps share the same color scale (where blue corresponds to low density and red corresponds to high density); the different interpolating step size, however, causes slightly different colors at their edge, around $H_m \sim 10$ kOe. While a finer interpolation step size is necessary to well visualize the peak in the low-field region, it is not adequate in the high-field region where data points are much sparser (with gaps as large as 40 kOe between some points) and a fine step interpolation would create artificial features.

The density map at low H_m shows a narrow high-density peak (red color) over a wide low-density background (blue

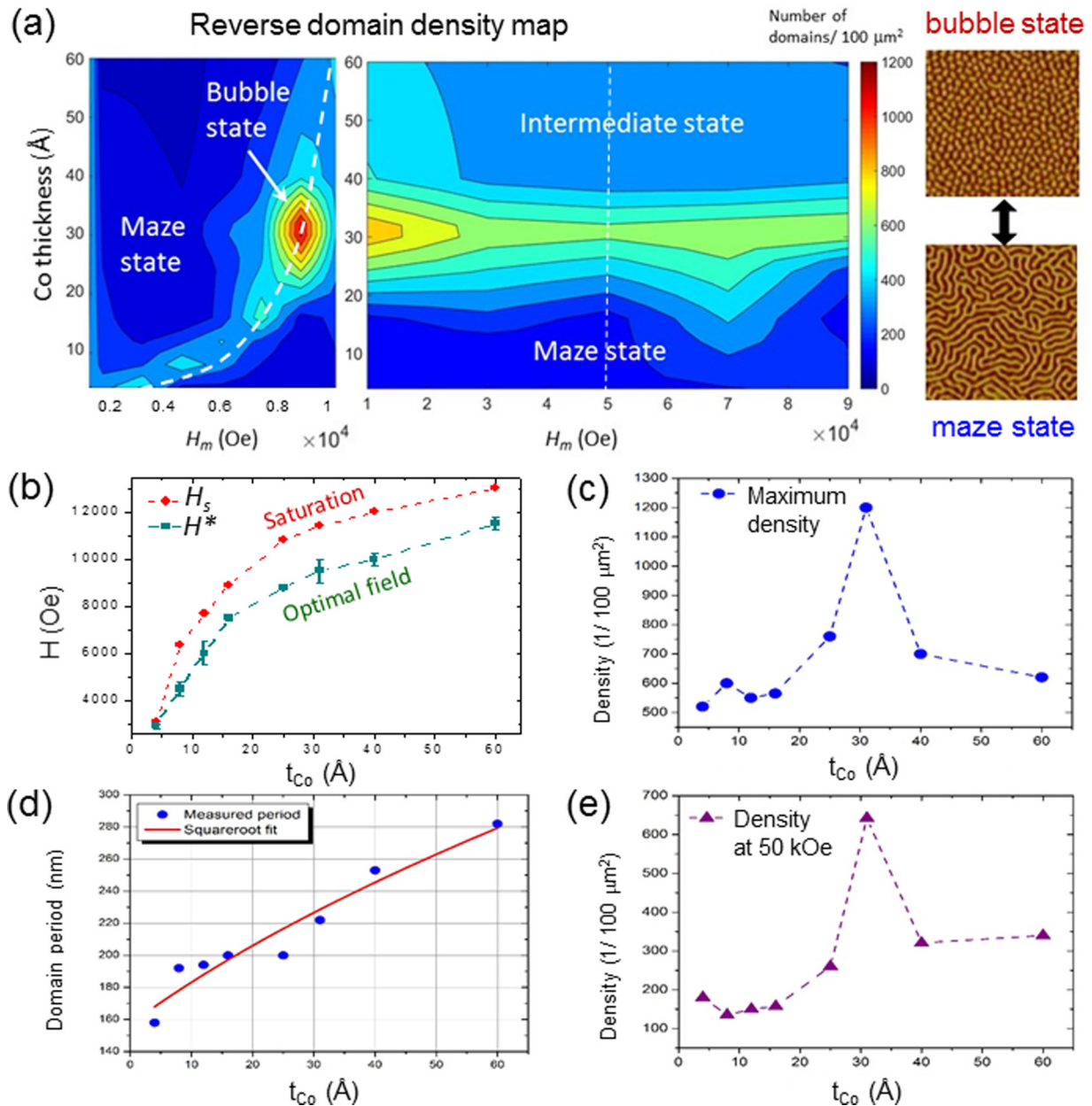


FIG. 7. Visualization of the morphological magnetic stripe-bubble transition. (a) Map of the density of the reverse domains at remanence as a function of H_m and Co thickness. Left portion: Low-field map (covering the range $0 < H_m < 10.5$ kOe) with fine interpolating step size ($\Delta H_m = 1.5$ kOe). Right portion: High-field map (covering the range $10 < H_m < 90$ kOe) with wide interpolating step size ($\Delta H_m = 20$ kOe). MFM images of a pure maze state and a pure bubble state are shown on the right side of the maps. (b) Plot of the optimal field H^* and the saturation field H_s as a function of Co thickness. (c) Optimal density n^* as a function of Co thickness. This curve corresponds to a cut through the left portion of the density map, along the dashed line. (d) Average period in the magnetic domain pattern vs Co thickness. The associated average magnetic domain size is basically half the period. This period was measured by Fourier transforming MFM images of mazelike patterns, thus providing a statistical average value. (e) Density n of the reverse magnetic domains in the remanent pattern after a major loop has been applied. This curve corresponds to a cut through the right portion of the density map (a) along the dashed line at $H_m \sim 50$ kOe.

color). The observed peak extends into a ridge towards higher fields $H_m > H_s$ prolonging parallel to the horizontal H_m axis. The height of this ridge, about 600 domains/ $100 \mu\text{m}^2$, is lower than the peak value (1200 domains/ $100 \mu\text{m}^2$) but still significantly higher than the baseline at low H_m . Everywhere in the low-density blue region, the domain pattern is mazelike with long interlaced stripe domains. At the peak of the high-

density region (red dot) the domain pattern has reached a bubble state, where domains have shrunk down to a minimum size. For the intermediate density regions (light blue to yellow color), the domain pattern is in an intermediate state, with a mix of bubbles and relatively short interlaced stripes.

The high-density peak in Fig. 7(a) (left) extends only over a small range of H_m values around H^* . This peak is prolonged

by a narrow curved tail at low Co thicknesses. In Fig. 7(b), the peak field H^* , along with the saturation field H_s , is plotted as a function of Co thickness. The trend followed by H^* mimics that of H_s , which is increasing as a function of Co thickness. For all the Co thicknesses, H^* is systematically slightly lower than H_s . The gap between H^* and H_s is relatively small (~ 200 Oe) for 4-Å Co, but increases to larger values (between 1500 and 2000 Oe) for larger Co thicknesses. Overall, the ratio H^*/H_s , however, remains within 75–95%.

The value H^* approximately matches the value H_m at which the minor loop opens and hysteresis starts to occur. Indeed, in order to favor an optimal high-density bubble state at remanence, the magnetic film must be previously magnetized to this specific point H^* slightly below saturation, where magnetic domains have irreversibly broken down into smaller domains [11,54]. At that point, some of the domains may have already been annihilated, but there is still a significantly large density of small bubbles left [as also observed for Co(4 Å)/Pt(7 Å), in Fig. 3 of Ref. [11] and Figs. 2, 3, and 5 of Ref. [54]]. The optimum reversal point H^* seems to coincide with the slope change observed for the smaller Co thicknesses on the ascending branch of the major magnetization loop, which marked a transition from contraction of stripe domains to annihilation of bubble domains on the way to saturation [54,55]. When the applied magnetic field H is decreased from H^* back down to zero, the existing distribution of irreversibly broken-up bubbles prevents the domains from coalescing back into long stripes and only allows the formation of short-sized stripe or bubble domains to fill the gaps [see Figs. 5(b) and 6(b)]. For larger Co

thicknesses that show the decay of stripes into lines of bubbles more pronounced, the effective OOP magnetic anisotropy is particularly weak, so that the energy cost associated with the formation of additional domain walls necessary for creating these lines of bubbles is relatively low and domain coalescence does not reoccur as one reduces the external field then back to remanence. In particular, once a bubble state of high density is formed, the bubbles will repel each other due to dipolar interactions, which will make the inverse process of bubble coalescence less favorable, such that the high bubble density is mostly maintained when returning to remanence [44,57,58]. The emergence of the corresponding bubble state region is illustrated in the schematic illustration of Fig. 8(a).

The observed morphological stripe-bubble magnetic transition is accompanied by a significant enhancement in the density of reverse domains. In Fig. 7(c), the maximum density n^* for the reverse domains is plotted as a function of Co thickness. Accordingly, when the Co thickness in the [Co/Pt]₅₀ multilayer is ~ 30 Å, it is possible to increase the domain density at remanence from about 150 domains/100 μm^2 (pure maze state) to about 1200 domains/100 μm^2 (pure bubble state) simply by adjusting the magnitude H_m of the previously applied field to an optimal value H^* .

While bubble domains are still observed for Co thicknesses larger than 31 Å, a significant decrease in the maximum density n^* , from 1200 domains/100 μm^2 at 31 Å of Co down to about 600 domains/100 μm^2 at higher Co thicknesses, occurs. This density drop is partly caused by the increase of the average domain width. Indeed, when the Co thickness increases from 31 to 40 Å, the average magnetic period

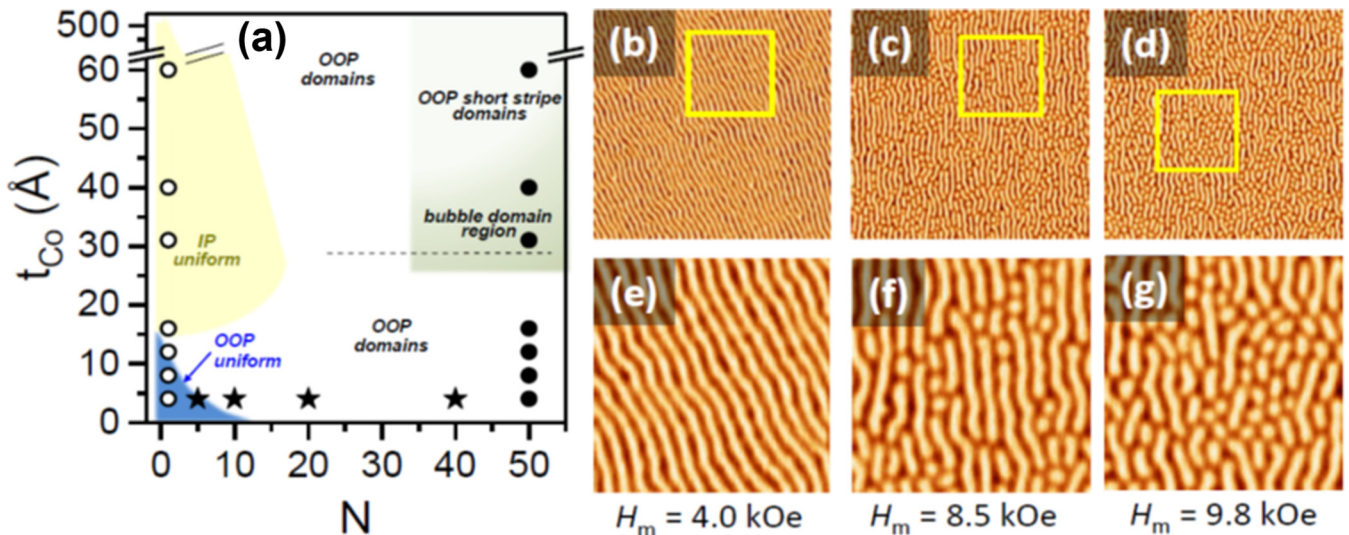


FIG. 8. (a) Replot of Fig. 1(d) with additional indication of the line for minimum effective perpendicular anisotropy (dashed line) that extends out roughly horizontally from the corner of the IP region at the highest N . This line represents the approximate phase region, where bubble domains are most likely to form. A bubble-rich state occurs not only when previously applying H^* [Fig. 7(c)], but also when previously saturating the films [Fig. 7(e)]. On the right in part (b)–(d) we show $10 \times 10 \mu\text{m}^2$ remanent MFM images that illustrate how the magnetic stripe domains decay into lines of bubbles in order to reduce their magnetization and magnetostatic energy. These images have been obtained for the Co(31 Å)/Pt(7 Å) sample after an external field was applied at an angle of 15° with respect to the OOP direction in order to trap mixed stripe-bubble states with stripe domains aligned to the direction of the IP component of the external field. Here the decay from stripes into bubbles is well visible and only possible because the domain-wall energy is very low (compare also to Refs. [11,54]). (e)–(g) Zoomed-in portions corresponding to the yellow frames in images (b)–(d), showing the details of the domain structures.

across an up/down domain pair slightly increases from 220 to 250 nm, as shown in Fig. 7(d) [12]. However, this increase in domain size, by a factor 1.15, only slightly contributes to reduce the domain density. It cannot account for the entirety of the density drop, from 1200 down to 700 domains/ $100 \mu\text{m}^2$, i.e., by about a factor of 2, when the thickness increases from 31 to 40 Å. This significant drop suggests the existence of an optimal Co thickness in the [Co/Pt]₅₀ multilayer, at around 30 Å, for which the density of reverse domains is significantly enhanced.

The existence of such an optimal Co thickness is confirmed by the occurrence of the ridge on the right side of the density map of Fig. 7(a) when $H_m \gg H^*$. This ridge indicates that the density of reverse domains in the remanent pattern after applying a saturating field is much higher for 31 Å of Co than for other thicknesses. A cut through the map at $H_m \sim 50$ kOe shown in Fig. 7(e) clearly shows once again a peak at 31 Å, where the domain density reaches about 650 domains/ $100 \mu\text{m}^2$. For smaller Co thicknesses, the density is down to about 150 domains/ $100 \mu\text{m}^2$, which corresponds to a maze pattern of long interlaced domains. For Co thicknesses higher than 31 Å, the density is slightly above 300 domains/ $100 \mu\text{m}^2$. At these higher densities, the magnetic pattern consists of a mix of short stripes (the length of which is less than 1 μm , on average) and bubbles (the diameter of which is around 150 nm).

To test the robustness of the bubble state occurring for the 31-Å Co thickness, the experiment was reproduced with an external field directed at a 15° angle away from the perpendicular direction, thus generating a small IP component while keeping a strong OOP component. The resulting remanent patterns shown in Fig. 8 exhibit stripes aligned along the direction of the IP field component. Even with this imposed IP alignment, the domain morphology evolves from elongated stripes toward a mix of much shorter stripes and bubbles when the OOP component of the field approaches H^* [Fig. 8(g)]. The gradual decay from aligned stripes into lines of bubbles is clearly visible here. A similar behavior of stripe domains that tend to decay into lines of bubbles was recently also observed in Fe/Gd multilayers as a function of field and temperature [59].

The occurrence of such an optimal Co thickness leading to a pure bubble lattice may be explained in terms of the competing magnetic energy terms. The subtle interplay between the demagnetization energy and the perpendicular anisotropy energy, which reflects itself in the domain-wall energy, leads to the formation of a bubble lattice when the Co thickness is in the range of 30 Å. Here the cost of forming additional domain walls when the field is ramped close to saturation and the stripe domains decay into lines of bubbles [Figs. 8(b)–8(e)] is very low, thus the lowest energy state at fields of $H_m = H^* \sim 85\% H_s$ leads to an almost perfect magnetic bubble state, which is mostly maintained also when returning to remanence [44,57,58] [Fig. 5(b)]. For lower Co thicknesses that yield a higher effective perpendicular anisotropy energy (and consequently a higher domain-wall energy) each stripe contracts down to very few or even only a single bubble, which leads to a very sparsely populated bubble assembly with large spaces in between bubbles, which then evolves back into more interconnected stripes when

brought back to remanence. Also for higher Co thicknesses (higher than the critical 30 Å) the effective anisotropy energy is increased due to the rising magnetocrystalline anisotropy energy, but this increase is very slow and thus bubble domain formation is still quite favorable (as also observed for the 40- and 60-Å samples). However, with increasing Co thickness the characteristic stripe width increases with the square root of the total magnetic film thickness [12], so that even if the bubble state remains similar in its arrangement the average bubble size will increase and thus slowly lower the domain density. This is why we see a maximum domain density around this specific Co thickness of about 30 Å for Co/Pt multilayers with 50 repeats. In order to illustrate this effect the line of minimum effective perpendicular anisotropy is drawn in Fig. 8(a) as a dashed line. This line extends out approximately horizontally towards higher N from the right side of the IP phase area, situated at around $N = 20$. The 30-Å Co thickness comes the closest to this line of lowest effective OOP anisotropy and thus reveals the most extensive bubble domain formation in our series.

VI. MICROMAGNETIC SIMULATIONS

Using MUMAX3 based finite-difference modeling [60] with periodic boundary conditions, we simulated the magnetic behavior of the $t_{\text{Co}} = 31$ Å sample by splitting up the thickness of the total multilayer into 20 cells of 9.25-nm thickness each (thus giving a total thickness of $20 \times 9.25 \text{ nm} = 185 \text{ nm}$). Furthermore, in order to capture domain states we used lateral cell sizes of $3 \text{ nm} \times 3 \text{ nm}$, i.e., with a length scale on the order of the exchange length in the system. For capturing at least a few domains (with a diameter of 200–300 nm) within the lateral size of our simulated area, we decided to use a $512 \times 512 \times 20$ cell grid with a lateral dimension of $1536 \text{ nm} \times 1536 \text{ nm}$. We chose the M_S value at 1080 kA/m as obtained from the VSM measurements. The PMA was varied across three values: $K_u = 2 \times 10^5$, 4×10^5 , and $6 \times 10^5 \text{ J/m}^3$. To obtain the hysteresis loop, the system was initialized using a random state and the total energy was minimized for every field step using a steepest-descent solver. We found quite close agreement of the modeled and measure hysteresis loop branch for $K_u = 2 \times 10^5 \text{ J/m}^3$ as shown in Figs. 9(a) and 9(b).

In Fig. 9(b) ascending hysteresis loop branches for all three modeled anisotropy values are shown together with the experimental branch of the $t_{\text{Co}} = 31$ Å multilayer, which was stretched by a small factor of 5% in order to confirm the good agreement between modeling and experiment for this anisotropy value.

The smallest simulated K_u value of $2 \times 10^5 \text{ J/m}^3$ matches our experimental results, thus confirming our above interpretation that the low anisotropy of the system triggers the extensive bubble domain formation. The magnetostatic energy for the same multilayer (with $M_S = 1080 \text{ kA/m}$) in a uniform OOP state would be three to four times larger than this value, thus yielding an IP state if no domain formation is allowed. However, including domain formation the system can reach an OOP domain ground state at remanence. Given that we had to stretch our experimental branch slightly by 5% in order to get full agreement as shown in Fig. 9(b), we can

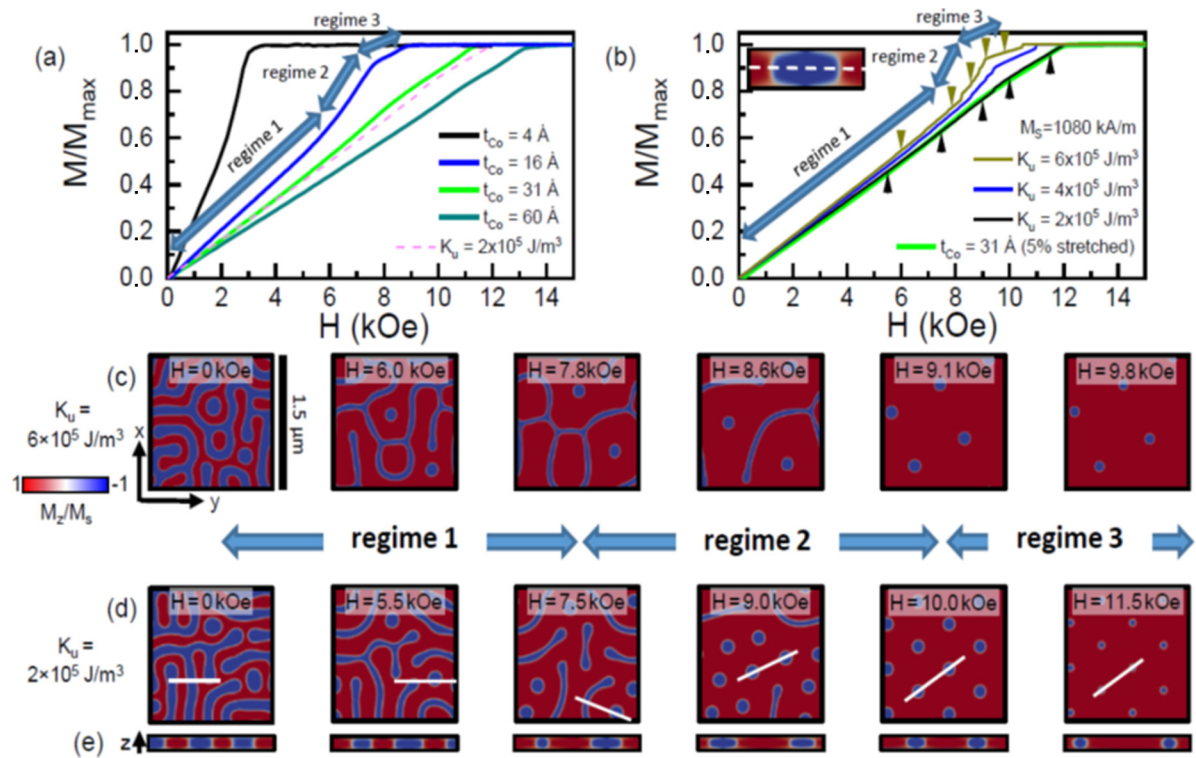


FIG. 9. (a) Experimental ascending hysteresis loop branches from remanence to saturation for four different Co thicknesses together with the corresponding modeled hysteresis loop branch for $M_S = 1080$ kA/m (as extracted for the sample with $t_{Co} = 31$ Å) and $K_u = 2 \times 10^5$ J/m³. (b) Modeled hysteresis loop branches from remanence to saturation for $M_S = 1080$ kA/m and three different K_u values together with the corresponding experimental hysteresis loop branch for $t_{Co} = 31$ Å stretched by 5% along the field axis in order to completely match with the model branch for $K_u = 2 \times 10^5$ J/m³. The inset in (b) shows a cross section through a domain modeled for $K_u = 2 \times 10^5$ J/m³, which shows extensive formation of IP closure domains (white areas). (c), (d) Modeled plan view domain images cut through the center of the magnetic multilayer structure [as indicated by the dashed line in the inset of (b)] for $K_u = 6 \times 10^5$ and 2×10^5 J/m³, respectively. The three different reversal regimes as identified for the $t_{Co} = 16$ Å sample and the $K_u = 6 \times 10^5$ J/m³ simulation are indicated in the ascending hysteresis loop branch in (a), (b) as well as in the domain images in (c), respectively. (e) One-dimensional cross-sectional cuts through the domain structures for $K_u = 2 \times 10^5$ J/m³ as indicated by the white solid lines in (d).

assume that our anisotropy for the $t_{Co} = 31$ Å multilayer lies slightly above $K_u = 2 \times 10^5$ J/m³.

If we inspect the other two loop branches with higher anisotropy values of $K_u = 4 \times 10^5$ and 6×10^5 J/m³ in Fig. 9(b), we note that the shape of these branches much more resembles that of the $t_{Co} = 16$ Å multilayer. For $K_u = 6 \times 10^5$ J/m³ we observe three different slope regimes [Fig. 9(b)] that correspond to different domain processes as illustrated in Fig. 9(c). First, starting at remanence a moderate slope (regime 1) with very little hysteresis is observed. This indicates reversible changes in relative domain width of up versus down domains (without changing the overall up/down domain period) induced by the Zeeman energy in the increasingly strong external field [11]. At some field value the domains that are opposite to the externally applied field cannot shrink in width any further [see image for 7.8 kOe in Fig. 9(c)]. At this point irreversible domain contraction processes from the end points of the stripe domains start to occur [see image for 8.6 kOe in Fig. 9(c)], which yield a higher $M(H)$ slope and a more hysteretic behavior (regime 2). Finally, when all the remaining stripes have contracted to bubbles [see image for 9.1 kOe in

Fig. 9(c)] the slope in the ascending hysteresis loop branch eventually decreases (reflecting bubble contraction, regime 3) before the system completely saturates and all remaining bubbles are annihilated. This sequence describes the reversal for higher anisotropy films that show less bubble domain formation, as seen in our sample series for Co thicknesses smaller than 30 Å.

In contrast to the $K_u = 6 \times 10^5$ J/m³ case, Fig. 9(d) shows domain images for the reversal at $K_u = 2 \times 10^5$ J/m³. In that case, the ascending branch of the hysteresis loop shows an almost constant slope. Here the change in magnetization versus field is almost linear all the way from remanence to saturation and also hysteresis is minimal. While the reversible up/down domain width changes in the first reversal phase are similar to the higher anisotropy samples, the second phase is different. Here a stripe domain no longer contracts down to a single bubble, but instead decays into short stripes and then a dense array of bubbles [see image for 9.0 and 10.0 kOe in Fig. 9(d)]. This way the slope change due to irreversible stripe domain contraction down to a single bubble is avoided and an almost linear regime all the way to saturation occurs. Also, close to saturation, the slope due to bubble contraction

is larger than for the higher anisotropy cases, simply because the bubble density is much larger.

Important to note is that the magnetization profile is not homogenous along the thickness of the sample. To minimize the magnetostatic energy but still provide the OOP alignment favored by the PMA, a flux-closure domain is formed within the film thickness [Fig. 9(e)]. This leads to an effective reduction of the volume of the bubble domain, and therefore provides a possible stable ground state consisting of densely packed bubble domains.

VII. CONCLUSION

We have identified a morphological magnetic stripe-bubble transition occurring for the remanent magnetic domain configuration in [Co/Pt]₅₀ multilayers. We varied the thickness of Co from 4 to 60 Å with a fixed Pt thickness of 7 Å. All these multilayers exhibit effective perpendicular magnetic anisotropy and form submicron-sized OOP magnetic domain patterns with various morphologies at remanence. For each thickness, a magnetic transition was observed when the magnitude H_m of the previously applied magnetic field was varied across a range of values from above to below saturation. The magnetic microstructure was characterized by collecting MFM images of the magnetic domain patterns at remanence after applying a magnetization loop of magnitude H_m decreasing from 90 kOe down to zero. The magnetic transition was identified by mapping out the density of the reverse domains as a function of H_m and of Co thickness. The resulting map [Fig. 7(a)] clearly shows a magnetic transition with the occurrence of a narrow high domain density peak in the midst of a wide low domain density background. The reverse domain density is highly enhanced from its lowest value of about 150 domains/100 μm^2 , which corresponds to a maze domain state, up to 1200 domains/100 μm^2 , which corresponds to a pure bubble state. For the [Co/Pt]₅₀ multilayers with a Pt thickness of 7 Å this significant enhancement occurs at a characteristic Co thickness of around 30 Å and at a characteristic value $H^* \sim 9.5$ kOe for the magnitude of the previously applied field H_m . Ranging within 75–95% of the saturation field H_s , the characteristic field value H^* corresponds to the point where we observe for lower Co thicknesses a slope change in the major loop [as can be seen in the insets of Figs. 3(a) and 4(a)] corresponding to a transition from contraction of stripe

domains to contraction and annihilation of bubble domains on the way towards saturation [55]. For higher Co thicknesses, H^* is the point where the magnetization loop opens up to its hysteretic region and stripes decay into lines of bubble domains that remain energetically stable, even if the sample is brought back to remanence. As we show in our discussion, the ability to build more domain walls and thus separate stripe domains into lines of bubbles (Fig. 8) in order to reduce the overall magnetization and magnetostatic energy only become energetically feasible if the domain-wall energy is very low, which is the case when the effective OOP anisotropy of the multilayer reaches a minimum (but without getting into the IP regime yet). In Fig. 8, we illustrated that, for multilayers with 50 repeats and a Pt thickness of 7 Å, this local minimum lies at a Co thickness of about 30 Å. A comparison between additional micromagnetic finite-difference simulations and our experimental results confirms our interpretation and allows us to assign an anisotropy of about $K_u = 2 \times 10^5$ J/m³ to the [Co(31 Å)/Pt(7 Å)]₅₀ multilayer, for which we observe the highest bubble domain density.

This observed morphological stripe-bubble transition demonstrates the ability to enhance domain densities at remanence in ferromagnetic thin Co/Pt multilayered films by optimizing the Co thickness in combination with finely adjusting the magnitude of the previously applied external magnetic field strength. Observed here in Co/Pt multilayers, such a morphological stripe-bubble transition in the remanent magnetic domain configuration may well be found in other thin-film systems with perpendicular magnetic anisotropy and prove itself as being useful for creating dense arrays of magnetic bubbles for future magnetic data computation and storage applications.

ACKNOWLEDGMENTS

We thank Philip Salter for help in developing the algorithm to statistically analyze the magnetic images. We thank Prof. Kent Gee for help in developing the code to map domain densities with variably spaced data points. This work was made possible thanks to Brigham Young University, Office of Research and Creative Activities funding. We thank Gabriel Sellge for help with x-ray-diffraction measurements and Attila Kákay for help with extracting the micromagnetic simulation data.

-
- [1] C. A. Fowler, Jr. and E. M. Fryer, *Phys. Rev.* **100**, 746 (1955).
 - [2] H. J. Williams and R. C. Sherwood, *J. Appl. Phys.* **28**, 548 (1956).
 - [3] J. N. Chapman, *J. Phys. D* **17**, 623 (1984).
 - [4] R. Allenspach, M. Stampanoni, and A. Bischof, *Phys. Rev. Lett.* **65**, 3344 (1990).
 - [5] P. Lecoeur, P. L. Trouilloud, G. Xiao, A. Gupta, G. Q. Gong, and X. W. Li, *J. Appl. Phys.* **82**, 3934 (1997).
 - [6] A. Lisfi and J. C. Lodder, *Phys. Rev. B* **63**, 174441 (2001).
 - [7] M. T. Johnson, P. J. H. Bloemen, F. J. A. den Broeder, and J. J. de Vriest, *Rep. Prog. Phys.* **59**, 1409 (1996).
 - [8] V. Gehanno, Y. Samson, A. Marty, B. Gilles, and A. Chamberod, *J. Magn. Magn. Mater.* **172**, 26 (1997).
 - [9] V. Gehanno, A. Marty, B. Gilles, and Y. Samson, *Phys. Rev. B* **55**, 12552 (1997).
 - [10] J.-U. Thiele, L. Folks, M. F. Toney, and D. K. Weller, *J. Appl. Phys.* **84**, 5686 (1998).
 - [11] O. Hellwig, G. P. Denbeaux, J. B. Kortright, and E. E. Fullerton, *Physica B* **336**, 136 (2003).
 - [12] O. Hellwig, A. Berger, J. B. Kortright, and E. E. Fullerton, *J. Magn. Magn. Mater.* **319**, 13 (2007).
 - [13] E. Y. Vedmedenko, A. Ghazali, and J.-C. S. Levy, *Phys. Rev. B* **59**, 3329 (1999).

- [14] A. Wachowiak, J. Wiebe, M. Bode, O. Pietzsch, M. Morgenstern, and R. Wiesendanger, *Science* **298**, 577 (2002).
- [15] K. Shigetou, T. Okuno, K. Mibu, and T. S. Ono, *Appl. Phys. Lett.* **80**, 4190 (2002).
- [16] X. Z. Yu, N. Kanazawa, Y. Onose, K. Kimoto, W. Z. Zhang, S. Ishiwata, Y. Matsui, and Y. Tokura, *Nature Mater.* **10**, 106 (2011).
- [17] M. N. Wilson, E. A. Karhu, A. S. Quigley, U. K. Rößler, A. B. Butenko, A. N. Bogdanov, M. D. Robertson, and T. L. Monchesky, *Phys. Rev. B* **86**, 144420 (2012).
- [18] A. Fert, V. Cros, and J. Sampaio, *Nature Nanotech.* **8**, 152 (2013).
- [19] W. Jiang, P. Upadhyaya, W. Zhang, G. Yu, M. B. Jungfleisch, F. Y. Fradin, J. E. Pearson, Y. Tserkovnyak, K. L. Wang, O. Heinonen, S. G. E. te Velthuis, and A. Hoffmann, *Science* **349**, 283 (2015).
- [20] N. S. Kiselev, A. N. Bogdanov, R. Schäfer, and U. K. Rößler, *J. Phys. D* **44**, 392001 (2011).
- [21] A. Fert, N. Reyren, and V. Cros, *Nat. Rev. Mater.* **2**, 17031 (2017).
- [22] J. J. Cuomo, P. Chaudhari, and R. J. Gambino, *J. Electronic Materials* **3**, 517 (1974).
- [23] K. Chesnel, in *Magnetism and Magnetic Materials*, edited by N. Panwar (InTechOpen, London, UK, 2018), Chap. 3.
- [24] M. Pierce, C. R. Buechler, L. B. Sorensen, J. J. Turner, S. D. Kevan, E. A. Jagla, J. M. Deutsch, T. Mai, O. Narayan, J. E. Davies, K. Liu, J. Hunter Dunn, K. M. Chesnel, J. B. Kortright, O. Hellwig, and E. E. Fullerton, *Phys. Rev. Lett.* **94**, 017202 (2005).
- [25] M. S. Pierce, J. E. Davies, J. J. Turner, K. Chesnel, E. E. Fullerton, J. Nam, R. Hailstone, S. D. Kevan, J. B. Kortright, K. Liu, L. B. Sorensen, B. R. York, and O. Hellwig, *Phys. Rev. B* **87**, 184428 (2013).
- [26] P. Kappenberger, S. Martin, Y. Pellmont, H. J. Hug, J. B. Kortright, O. Hellwig, and E. E. Fullerton, *Phys. Rev. Lett.* **91**, 267202 (2003).
- [27] K. Chesnel, E. E. Fullerton, M. J. Carey, J. B. Kortright, and S. D. Kevan, *Phys. Rev. B* **78**, 132409 (2008).
- [28] K. Chesnel, A. Safsten, M. Rytting, and E. E. Fullerton, *Nature Comm.* **7**, 11648 (2016).
- [29] C. Banerjee, P. Gruszecki, J. W. Klos, O. Hellwig, M. Krawczyk, and A. Barman, *Phys. Rev. B* **96**, 024421 (2017).
- [30] M. Hoffmann, B. Zimmermann, G. P. Müller, D. Schürhoff, N. S. Kiselev, C. Melcher, and Stefan Blügel, *Nat. Comm.* **8**, 308 (2017).
- [31] S. Bordács, A. Butykai, B. G. Szigeti, J. S. White, R. Cubitt, A. O. Leonov, S. Widmann, D. Ehlers, H.-A. Krug von Nidda, V. Tsurkan, A. Loidl, and I. Kézsmárki, *Sci. Rep.* **7**, 7584 (2017).
- [32] J. Gao, S. Tanga, Y. Li, W. Xia, T. Tang, and Y. Du, *J. Appl. Phys.* **112**, 073913 (2012).
- [33] C. J. Lin, G. L. Gorman, C. H. Lee, R. F. C. Farrow, E. E. Marinero, H. V. do, H. Notarys, and C. J. Chien, *J. Magn. Magn. Mat.* **93**, 194 (1991).
- [34] P. F. Carcia, *J. Appl. Phys.* **63**, 5066 (1988).
- [35] G. Winkler, A. Kobs, A. Chuvilin, D. Lott, A. Schreyer, and H. P. Oepen, *J. Appl. Phys.* **117**, 105306 (2015).
- [36] F. J. A. den Broeder, D. Kuiper, A. P. van de Mosselaar, and W. Hoving, *Phys. Rev. Lett.* **60**, 2769 (1988).
- [37] C. Chappert, D. Renard, P. Beauvillain, J. P. Renard, and J. Seiden, *J. Magn. Magn. Mat.* **54-57**, 795 (1986).
- [38] C. Chappert and P. Bruno, *J. Appl. Phys.* **64**, 5736 (1988).
- [39] D. Weller, R. F. C. Farrow, R. F. Marks, G. R. Harp, H. Notarys, and G. Gorman, *Mater. Res. Soc. Symp. Proc.* **313**, 791 (1993).
- [40] M. Kisielewski, A. Maziewski, M. Tekielak, J. Ferrù, S. Lemerle, V. Mathet, and C. Chappert, *J. Magn. Magn. Mater.* **260**, 231 (2003).
- [41] Z. Malek and V. Kambersky, *Czech. J. Phys.* **8**, 416 (1958).
- [42] R. Allenspach and M. Stampanoni, in *Magnetic Surfaces, Thin Films, and Multilayers*, edited by S. S. P. Parkin *et al.*, MRS Symposia Proc. No. 231 (Materials Research Society, Pittsburgh, 1992), p. 17.
- [43] C. Kittel, *Phys. Rev.* **70**, 965 (1946).
- [44] M. Hehn, S. Padovani, K. Ounadjela, and J. P. Bucher, *Phys. Rev. B* **54**, 3428 (1996).
- [45] M. Hehn, K. Cherifi-Khodjaoui, K. Ounadjela, J. P. Bucher, and J. Arabski, *J. Magn. Magn. Mat.* **165**, 520 (1997).
- [46] J. Brandenburg, R. Hühne, L. Schultz, and V. Neu, *Phys. Rev. B* **79**, 054429 (2009).
- [47] O. Donzelli, M. Bassani, F. Spizzo, and D. Palmieri, *J. Magn. Magn. Mat.* **320**, e261 (2008).
- [48] L. Fallarino, O. Hovorka, and A. Berger, *Phys. Rev. B* **94**, 064408 (2016).
- [49] A. K. Suszka, A. Etxebarria, O. Idigoras, D. Cortés-Ortuño, P. Landeros, and A. Berger, *Appl. Phys. Lett.* **105**, 222402 (2014).
- [50] D. J. Craik and P. V. Cooper, *Phys. Lett.* **41A**, 255 (1972).
- [51] H. Stillrich, C. Menk, R. Frömter, and H. P. Oepen, *J. Appl. Phys.* **105**, 07C308 (2009).
- [52] J.-W. Lee, J.-R. Jeong, S.-C. Shin, J. Kim, and S.-K. Kim, *Phys. Rev. B* **66**, 172409 (2002).
- [53] R. Frömter, H. Stillrich, C. Menk, and H. P. Oepen, *Phys. Rev. Lett.* **100**, 207202 (2008).
- [54] J. E. Davies, O. Hellwig, E. E. Fullerton, G. Denbeaux, J. B. Kortright, and K. Liu, *Phys. Rev. B* **70**, 224434 (2004).
- [55] O. Hellwig, S. Eisebitt, W. Eberhardt, J. Lüning, W. F. Schlotter, and J. Stöhr, *J. Appl. Phys.* **99**, 08H307 (2006).
- [56] A. Westover, K. Chesnel, K. Hatch, P. Salter, and O. Hellwig, *J. Magn. Magn. Mater.* **399**, 164 (2016).
- [57] S. H. Charap and J. M. Nemchik, *IEEE Transactions on Magnetism, Mag.* **5**, 566 (1969).
- [58] J. A. Cape and G. W. Lehman, *J. Appl. Phys.* **42**, 5732 (1971).
- [59] S. A. Montoya, S. Couture, J. J. Chess, J. C. T. Lee, N. Kent, D. Henze, S. K. Sinha, M.-Y. Im, S. D. Kevan, P. Fischer, B. J. McMorran, V. Lomakin, S. Roy, and E. E. Fullerton, *Phys. Rev. B* **95**, 024415 (2017).
- [60] A. Vansteenkiste, J. Leliaert, M. Dvornik, M. Helsen, F. Garcia-Sanchez, and B. V. Waeyenberge, *AIP Advances* **4**, 107133 (2014).